Precise Measurement of Protein Interacting Fractions with Fluorescence Lifetime Imaging Microscopy

Kirstin A. Walther, Björn Papke, Maja B. Sinn, Kirsten Michel, and Ali Kinkhabwala

Supplementary figures and tables:

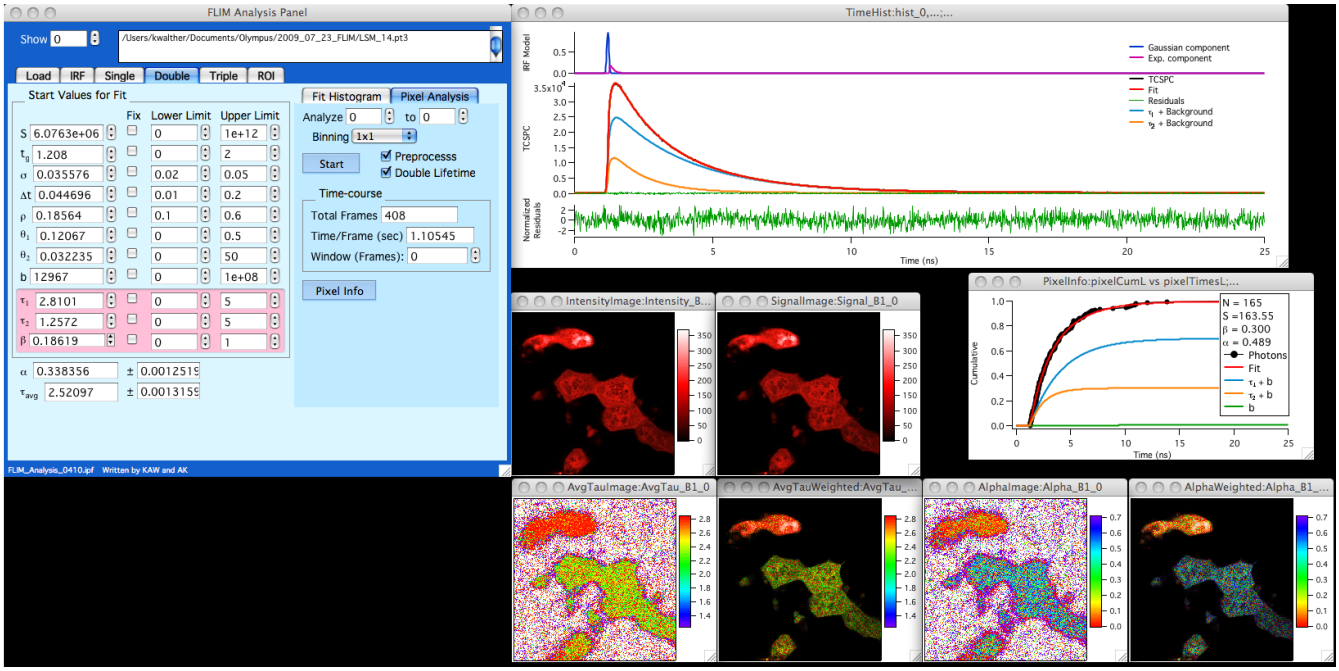

Fig. S1 Custom-written FLIM analysis program "*p*FLIM". Screenshot of our GUI-based FLIM analysis program written within the IgorPro environment. One or more data sets are loaded from the raw data acquisition files, which contain the absolute and pulse-relative arrival times and the arrival pixel for each photon. On a 2.33 GHz iMac, TCSPC χ^2 fitting to one histogram ($N = 5 \times 10^6$ counts in 1562 bins) takes only a few seconds and single pixel fitting for the entire 512×512 image takes roughly 30 s. Global fitting options are also included (not shown) for joint fitting of parameters across multiple images or image partitions (different ROIs and/or time slices).

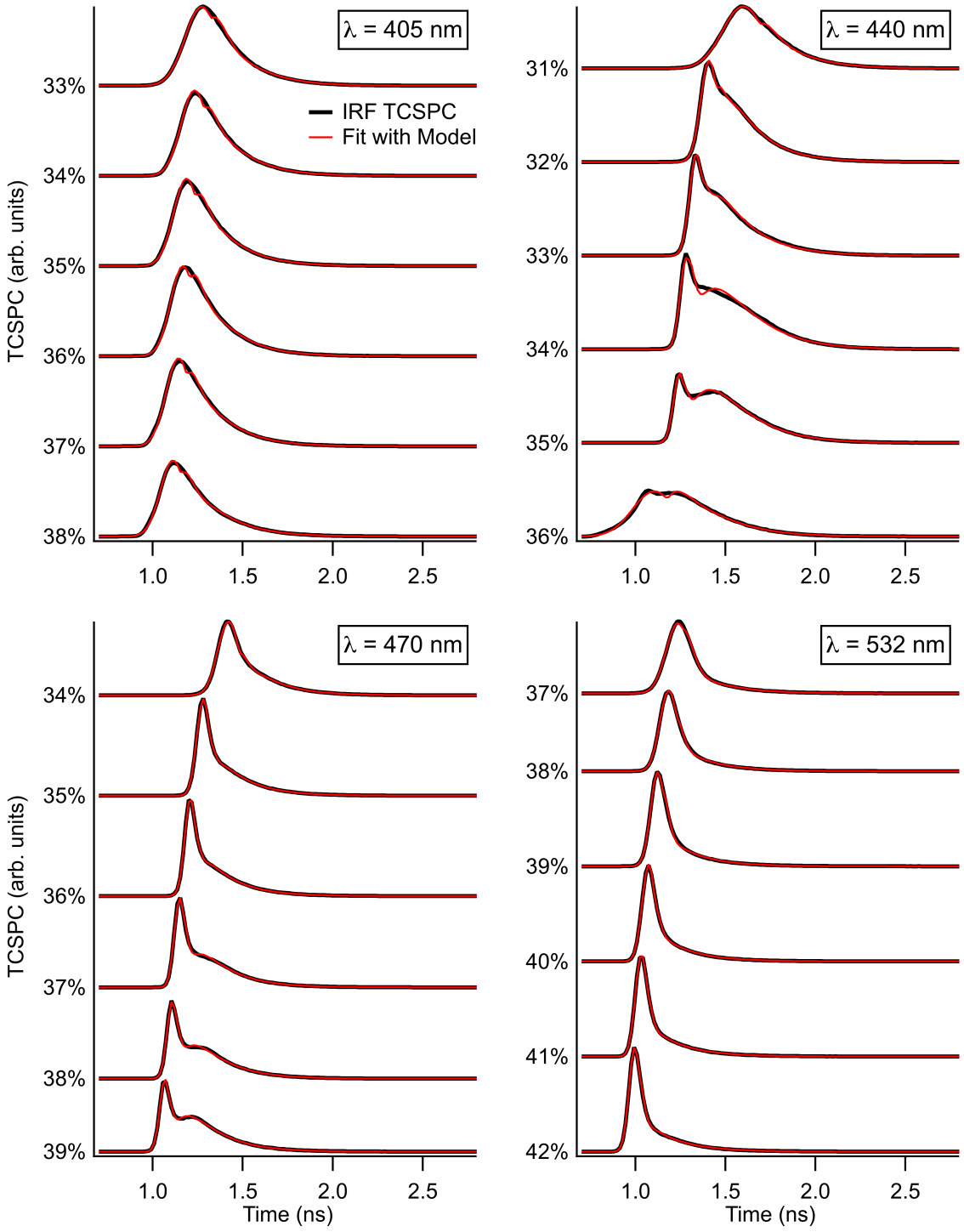

Fig. S2 IRF model fits to scattering-based IRF estimates. IRF model fits (red curves) overlaid on observed IRF estimates (black curves) obtained by direct detection of scattered excitation light. For each separate pulsed diode laser (405 nm, 440 nm, 470 nm, and 532 nm), the top curve corresponds to the minimal power at which lasing occurs and the successive lower curves correspond to increasing laser powers (up to 5% above the lasing threshold). The 470 nm IRF estimate at 36% power is also displayed in the inset of Fig. 1a.

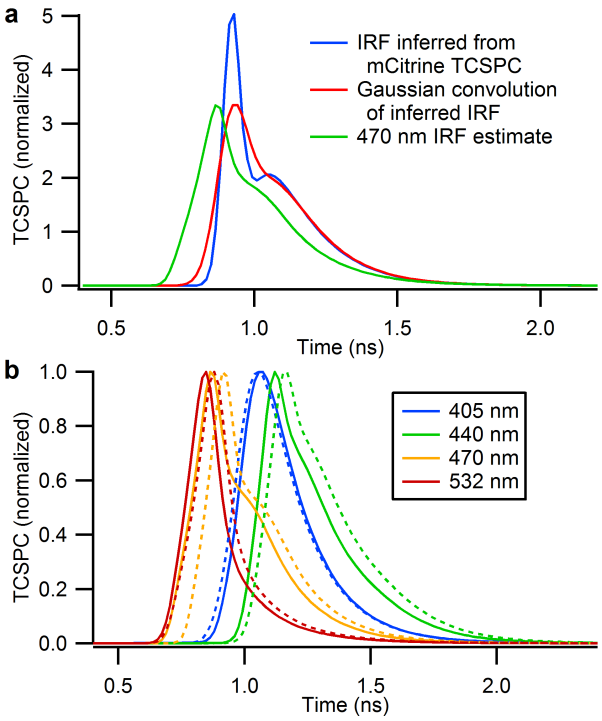

Fig. S3 Comparison of scattering-based IRF estimate with inferred IRF and IRF wandering. **(a)** IRF scattering-based estimate of the 470 nm pulsed laser (green curve) overlaid on an inferred IRF (blue curve) obtained from a fit to actual data, specifically, the biexponential fit to *in vitro* mCitrine (Figs. 3a and S11). Simple Gaussian convolution ($\sigma = 0.06$ ns) of the inferred IRF recorded between 500-550 nm (red curve) reproduced well the expected degradation (due to the known wavelength-dependent response of the detector) in the temporal resolution of the IRF estimate observed at the shorter wavelength of 470 nm. The mCitrine data set was taken 75 min after the IRF estimate using the same laser power (2% above the lasing threshold). The temporal offset of the green and red curves emphasizes the significance of IRF drift or wandering (see next panel). All IRF profiles were integral normalized to 1. **(b)** Scattering-based IRF estimates for each laser line were obtained (solid lines) and then retaken after a roughly three hour delay (dashed lines). IRF drift was observed for all lasers, and ranged up to ~ 0.1 ns. All IRF profiles have been peak normalized.

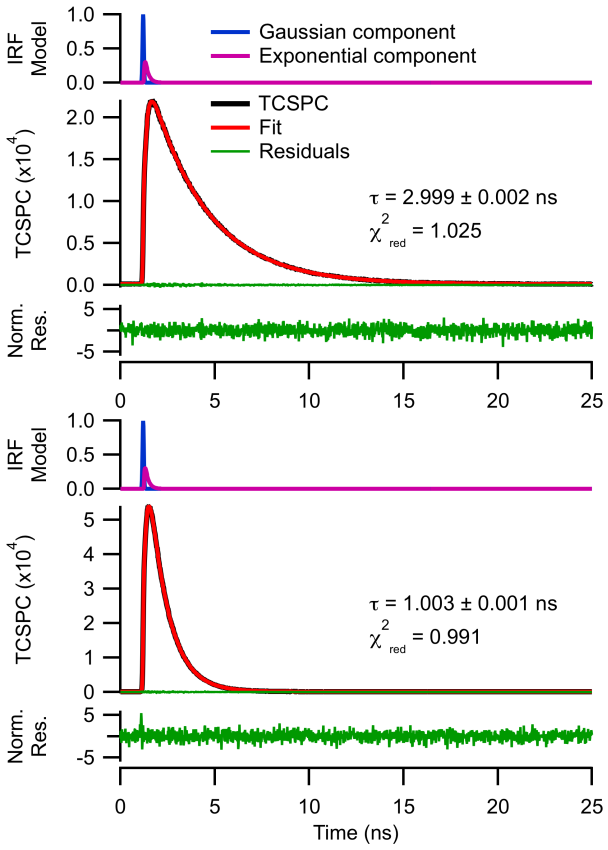

Fig. S4 TCSPC χ^2 fits to Monte Carlo monoexponential decays. χ^2 fits of our TCSPC model to monoexponential data generated by Monte Carlo ($N = 5 \times 10^6$, 3% flat background) using the observed scattering-based IRF estimate of the 470 nm laser at 36% power (Fig. S2). Fits are shown for lifetimes of 3 ns (top) and 1 ns (bottom). Lifetimes obtained from each fit (along with 1σ error bars and corresponding value of χ^2_{red}) are shown in the panels. IRFs inferred for each fit match very well the input IRF profile (not shown).

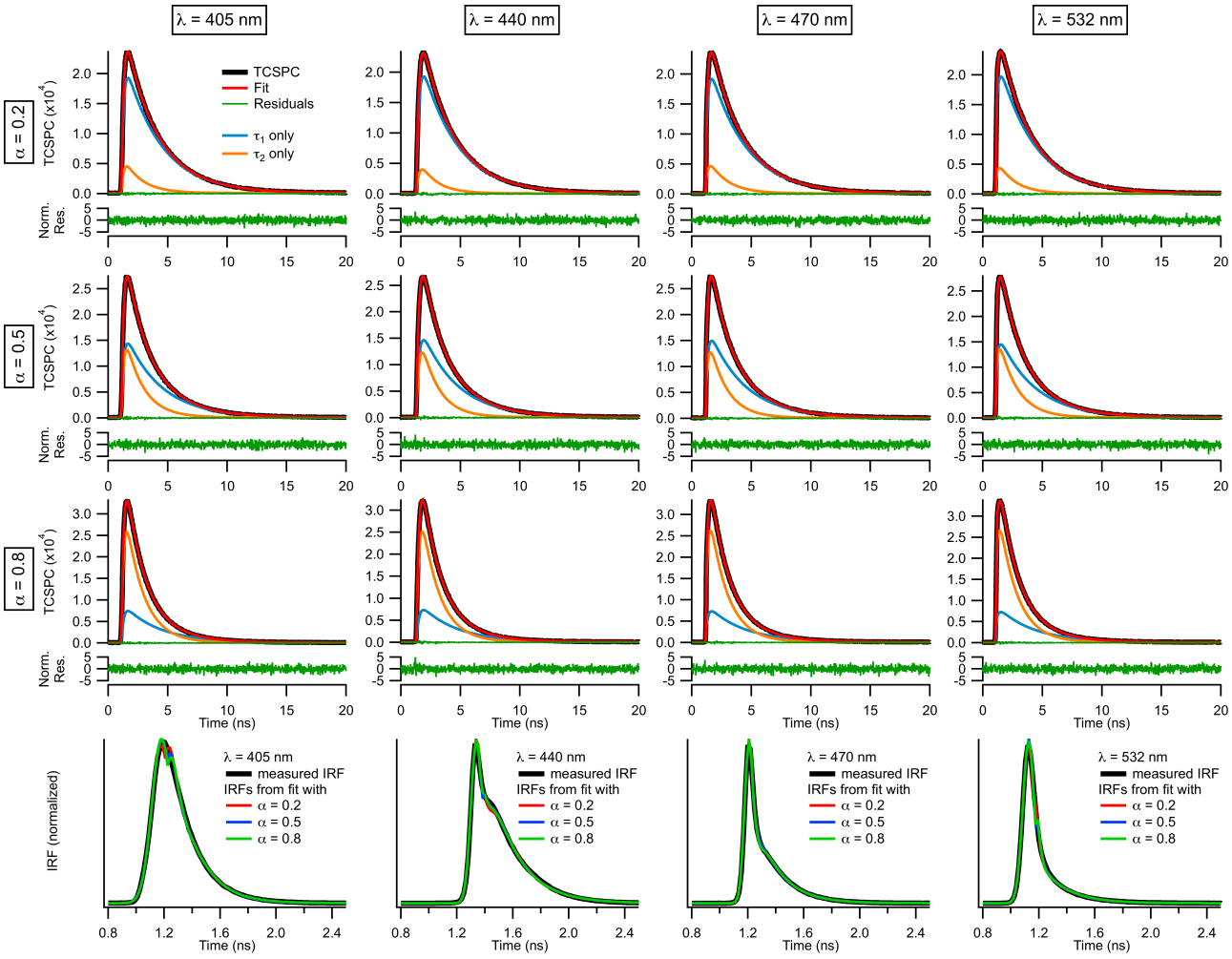

Fig. S5 TCSPC biexponential χ^2 fits to Monte Carlo biexponential decays. χ^2 fits of our biexponential TCSPC model to biexponential data generated by Monte Carlo ($N = 5 \times 10^6$, 3% flat background). Scattering-based IRF estimates for each excitation wavelength (Fig. S2, corresponding to 2% above the lasing threshold) were convolved with the two lifetimes $\tau_1 = 3$ ns and $\tau_2 = 1.5$ ns with different indicated FRET fractions, α, to generate the data shown in black. The model obtained by minimizing χ^2 is shown in red. Fitted values, along with 1σ errors, are given for τ_1, τ_2 and α for each simulation in Table S1. In the bottom row, the inferred IRFs for each α are overlaid on the specific scattering-based IRF estimate used for the Monte Carlo simulation.

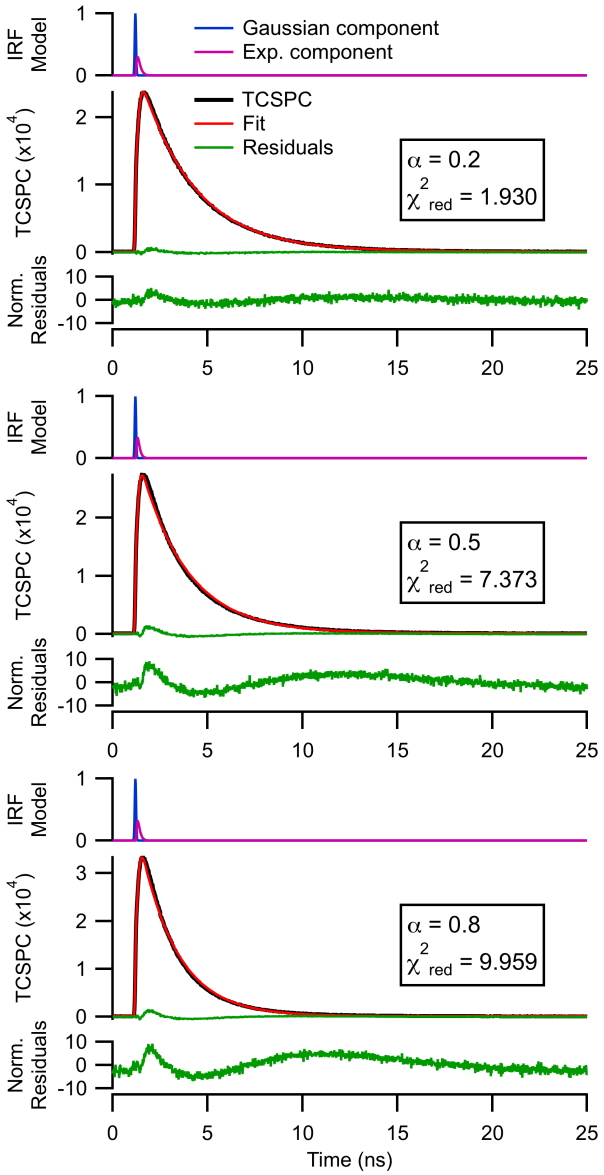

Fig. S6 TCSPC monoexponential χ^2 fits to Monte Carlo biexponential decays. χ^2 fits of our monoexponential TCSPC model (red curves) to biexponential data generated by Monte Carlo for the 470 nm laser (black curves, same $N = 5 \times 10^6$ count data as in Fig. S5). Very similar deviations in the residuals and χ^2_{red} values were obtained for the other lasers (not shown).

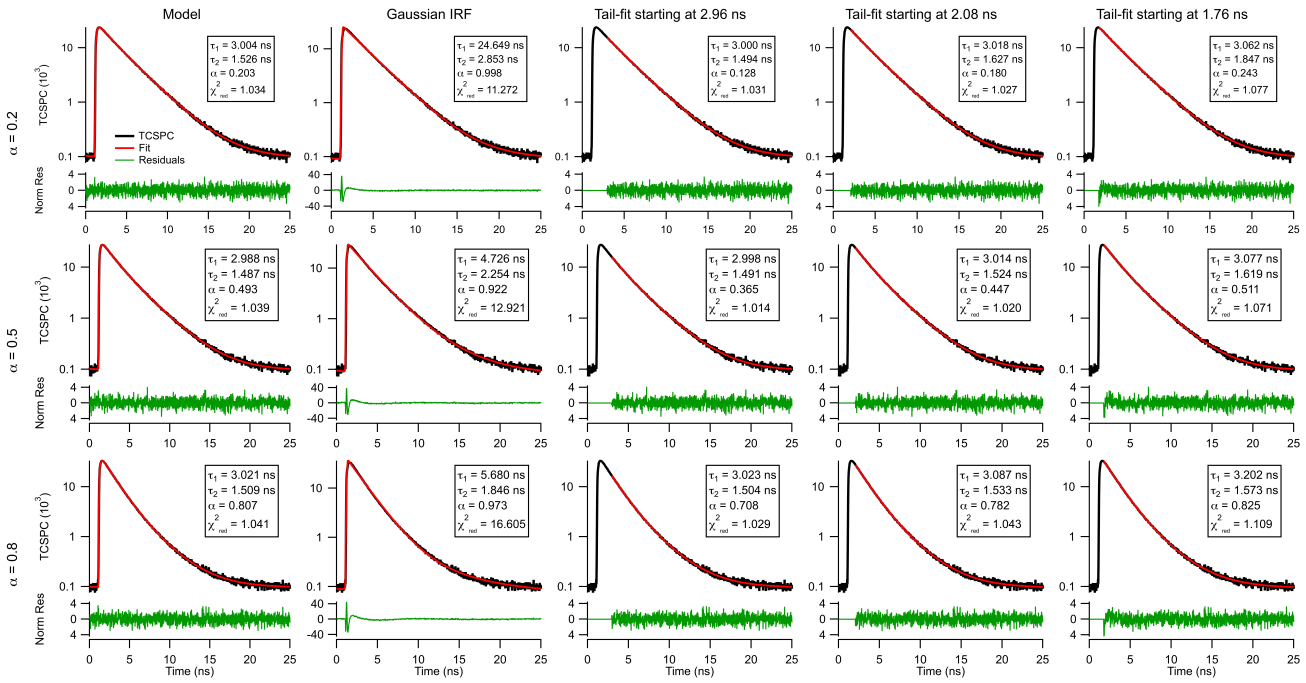

Fig. S7 Comparison of our TCSPC χ^2 fits with "Gaussian-only IRF" or "tail-fitting". Our biexponential χ^2 fits from Fig. S5 for the 470 nm laser (36%) are redisplayed in log units in the first column for $\alpha = 0.2\,(\text{top}), 0.5\,(\text{middle}), 0.8\,(\text{lower})$. χ^2 fit results, upon the assumption of a simpler Gaussian-only IRF (for which the secondary IRF component was set to zero and the IRF Gaussian arrival time t_0 and width σ were free to vary along with the decay parameters), are displayed in the second column. Results of tail-fitting for different choices of the beginning of the tail are shown in the third through fifth columns.

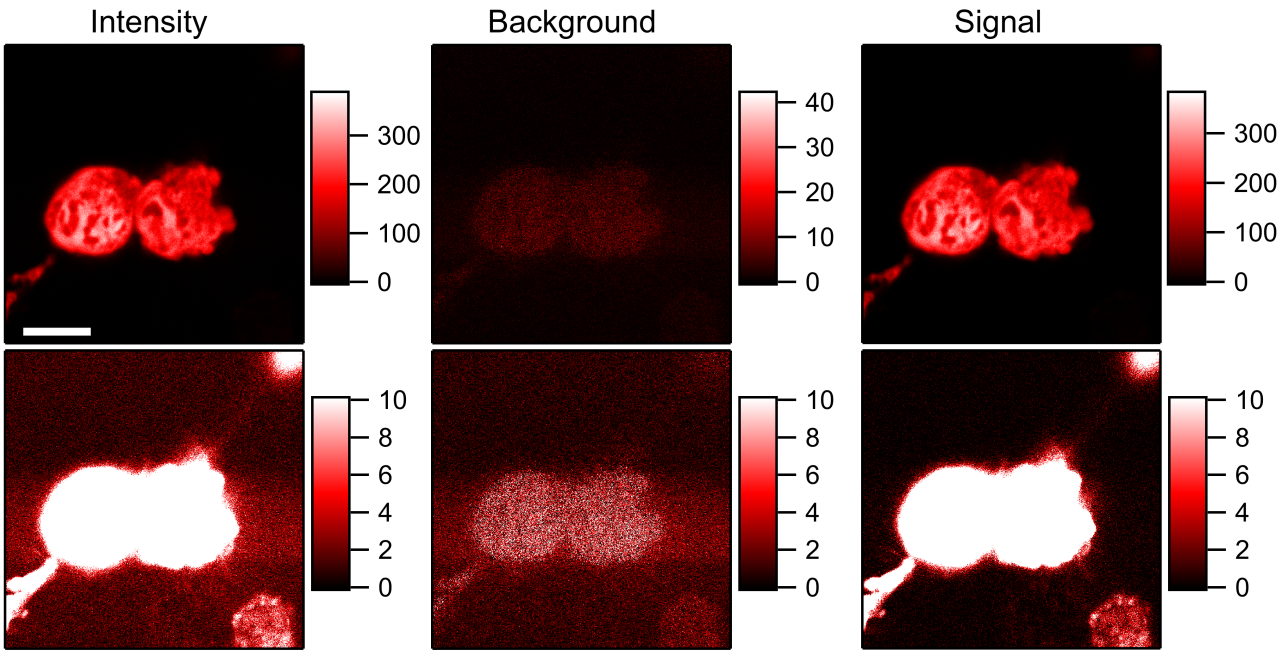

Fig. S8 Pixel-by-pixel differences in background. The total intensity image (512×512 image with 2 μs/pixel/scan) of two cells are shown in the top left, with a different upper limit on the color scale in the bottom left that reveals the contribution from dark counts (noticeable above and below the cells) and smearing of the image to the right and continuing on the left due to detector afterpulsing events. Application of our single pixel fitting analysis decomposes the total intensity image into background (middle; top and bottom) and signal (right; top and bottom) images. Afterpulsing of the detectors results in an increased occurrence of spurious background counts primarily within bright pixels but also immediately after scanning through such pixels, resulting in the observed image smearing to the right and continuing to the left on the next scanned line. Background events are efficiently removed from the final signal image both above and below the cells (primarily dark counts) and to the left and right of the cells (dark counts plus afterpulsing events). Background events are accounted for within the cells as well, resulting in the estimate S of the total signal counts compared to the observed count N in the pixel (see Fig. 1c). While these events represent only a few percent of the total counts, their random arrival times within the 25 ns pulse window can still significantly bias lifetime estimation for both bright and dim pixels (especially for dim pixels scanned immediately after bright pixels).

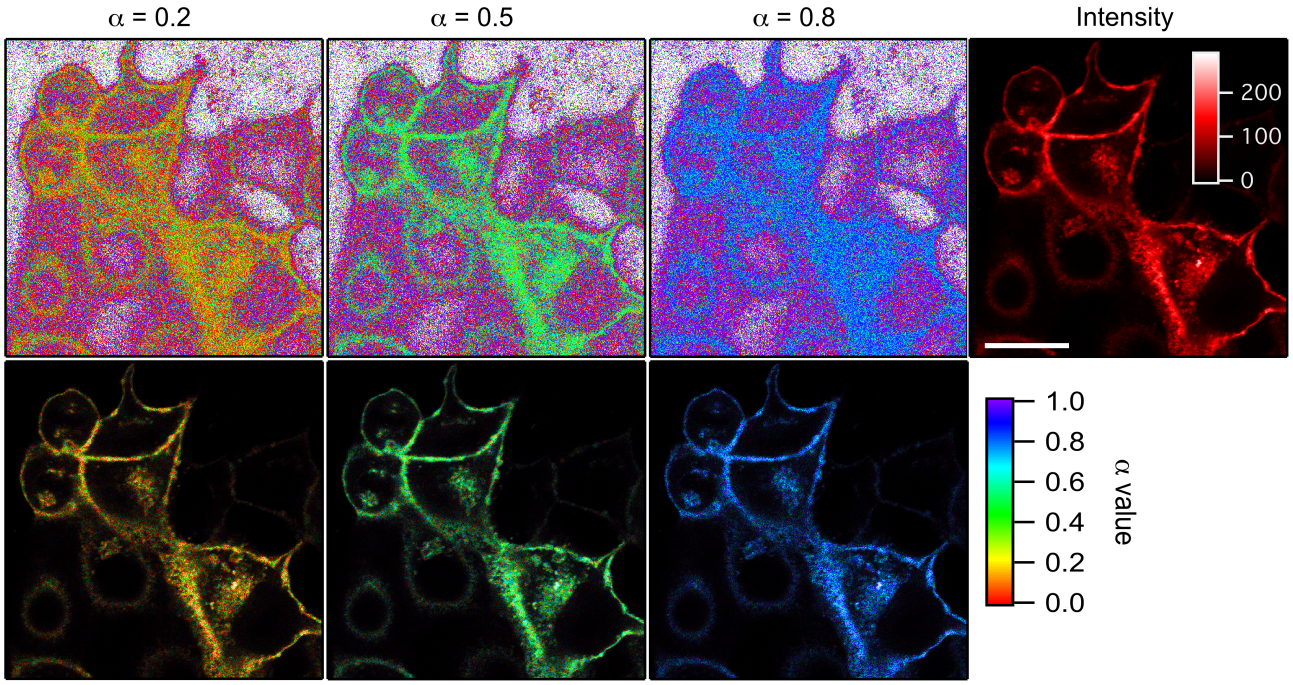

Fig. S9 Single pixel fitting of Monte Carlo biexponential data. The Monte Carlo generated data for the 470 nm laser shown in Fig. S5 were partitioned across the pixels of a previously-taken image of live cells. Replacement of the actual observed arrival times by the Monte Carlo arrival times allowed us to generate realistic images of cells for which the general reliability of the single-pixel fitting of lifetimes could be easily assessed. Each pair of images (α image and signal-weighted α image) corresponds to the biexponential histograms shown in Fig. S5.

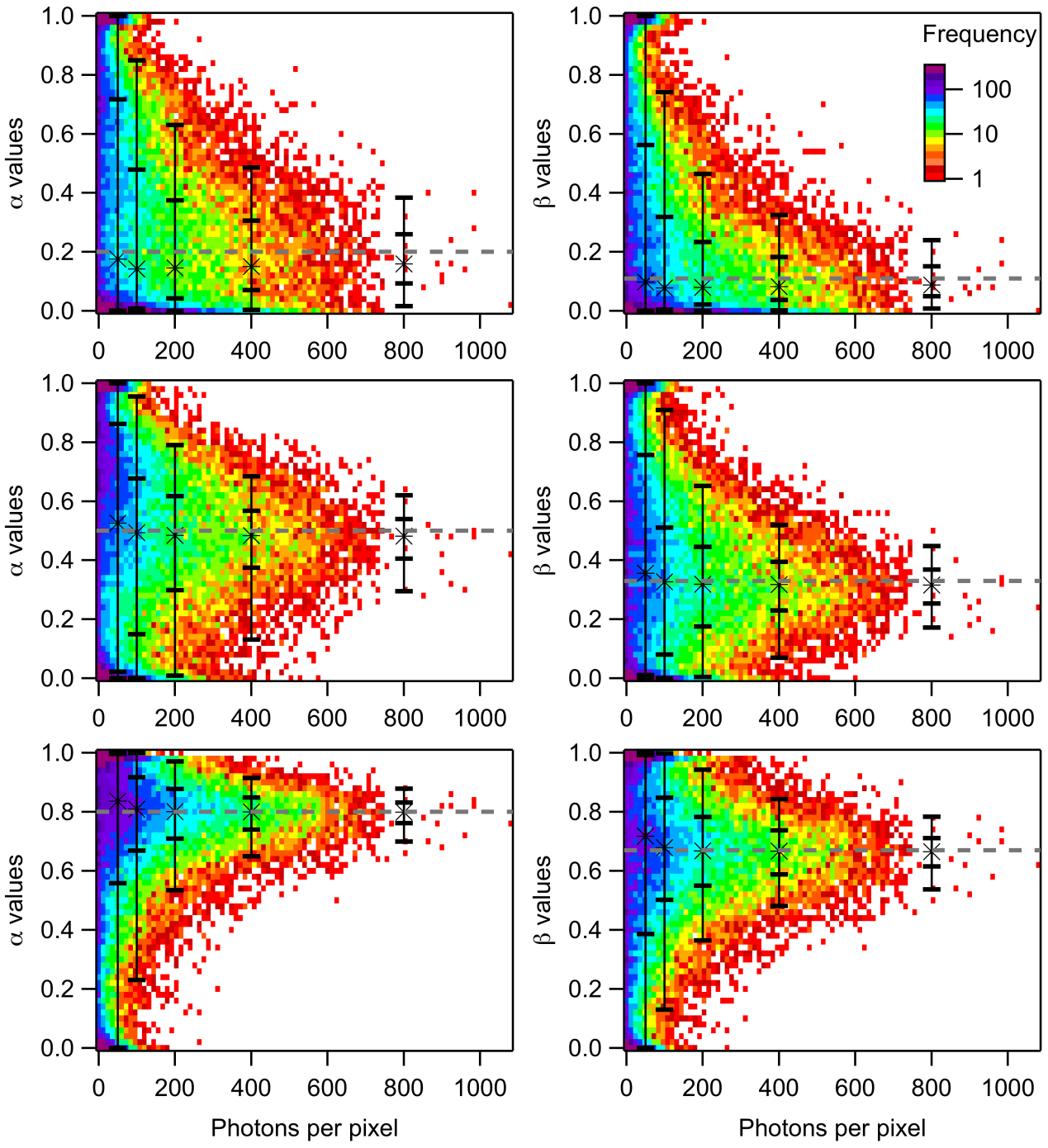

Fig. S10 Reliability of single pixel determination of FRET fraction. Single pixel estimates of the Monte Carlo image data for the 470 nm excitation laser (Fig. S5) are redisplayed as a function of pixel intensity from top-to-bottom: $\alpha = 0.2$ ($\beta = 0.111$), $\alpha = 0.5$ ($\beta = 0.333$), and $\alpha = 0.8$ ($\beta = 0.667$). A logarithmic color scale is used to provide more contrast. Superimposed confidence levels (5%, 25%, 50% (median), 75%, 95%) were obtained by additional Monte Carlo simulations, in which the $N = 5 \times 10^6$ events were partitioned into pixels that all had the same specified number of counts (either 50, 100, 200, 400, or 800 counts pixel^{-1}). Even for pixels containing less than 100 counts, lifetime discrimination is still statistically possible.

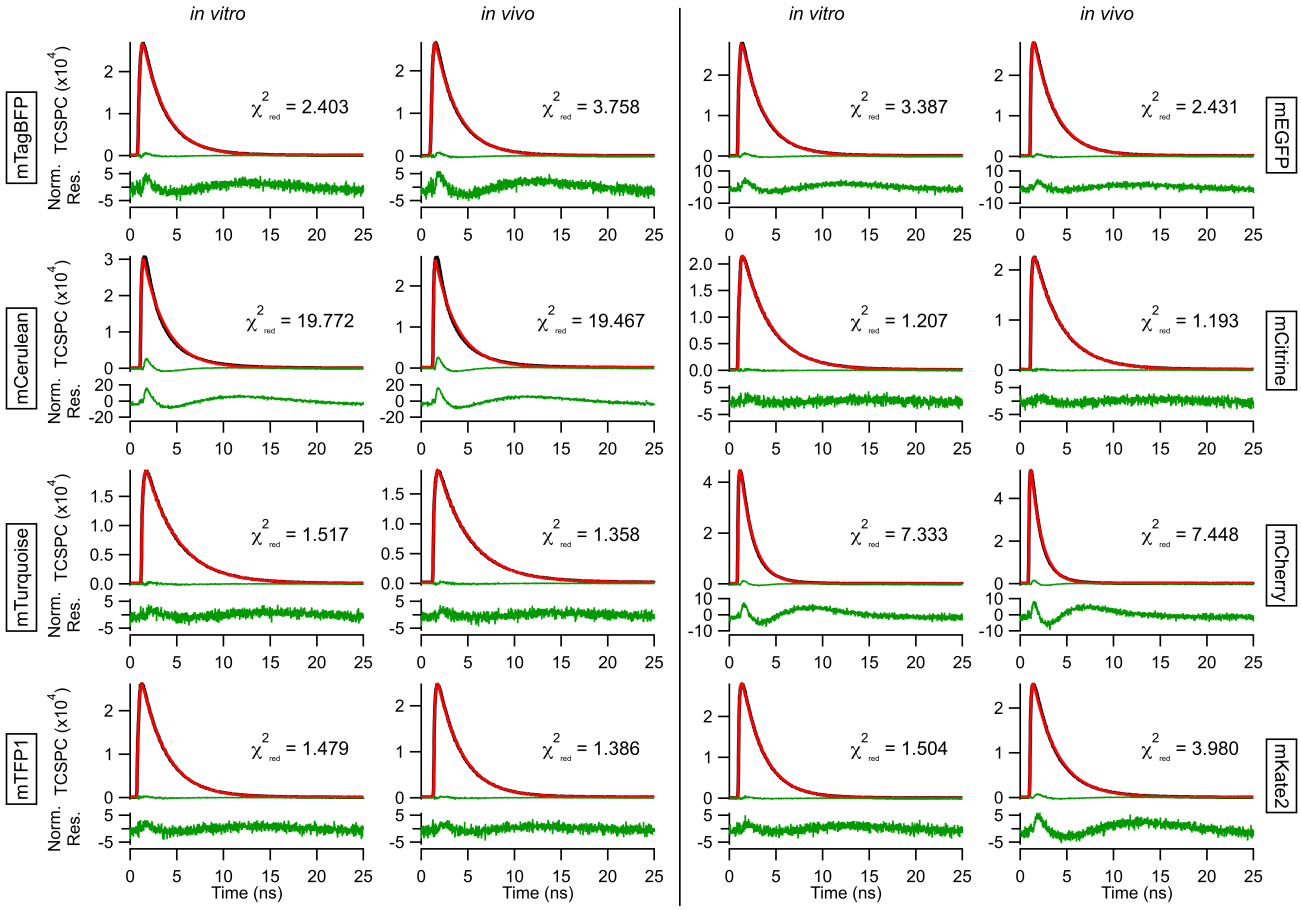

Fig. S11 TCSPC monoexponential χ^2 fits to fluorophore decays *in vitro* and *in vivo*. Histograms for each fluorophore *in vitro* at pH 9 and 37 °C (first and third columns) and *in vivo* at 37 °C (second and fourth columns) are fitted with our monoexponential model (see also Table 1). All TCSPC histograms contain $N \simeq 5 \times 10^6$ allowing direct comparison of the statistics across all of the fluorophore results as well as with the Monte Carlo results in Figs. S4-S6.

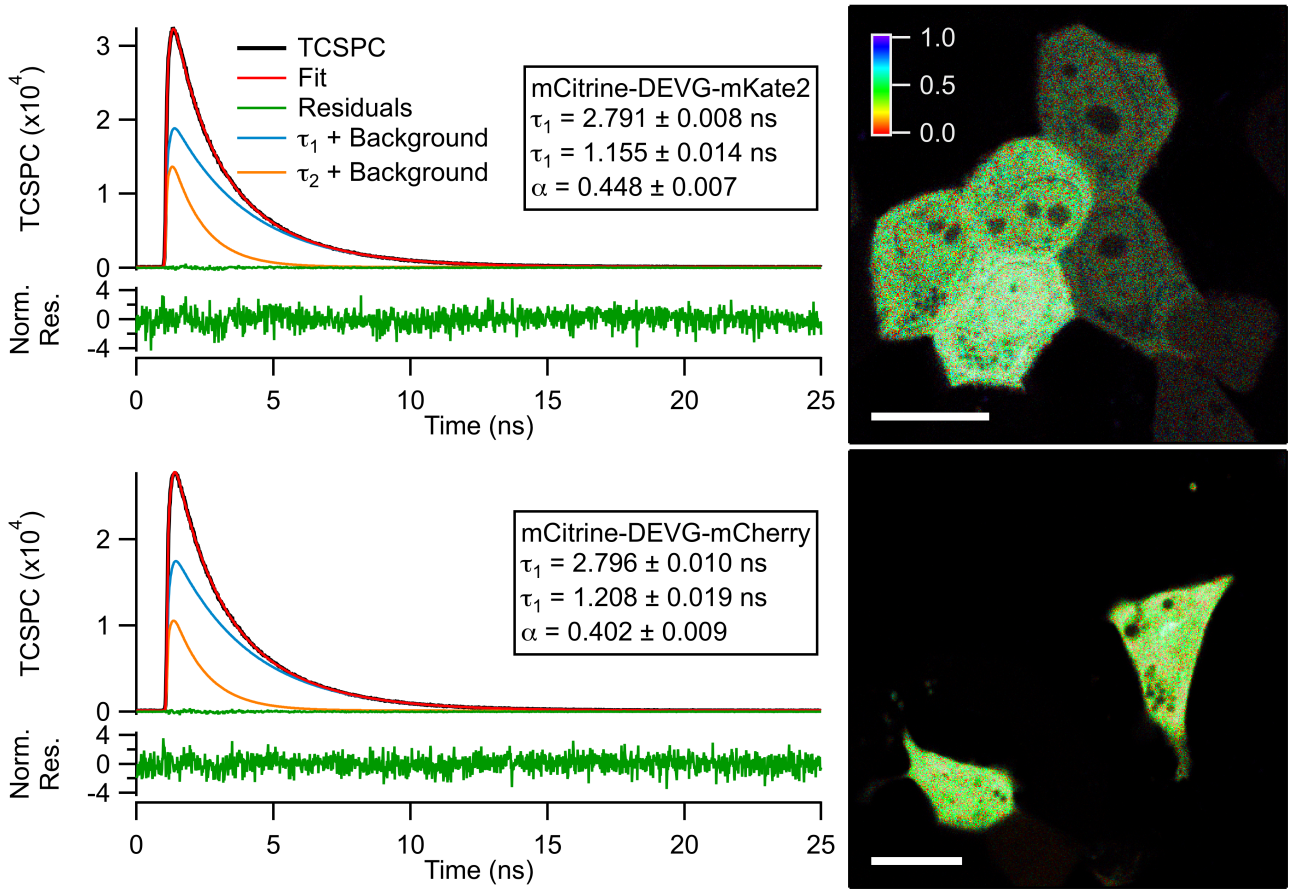

Fig. S12 TCSPC χ^2 fits and images of the FRET fraction for tandem fluorophore constructs. TCSPC χ^2 fits for MDCK cells expressing donor/acceptor pairs joined by an uncleavable linker. Top, mCitrine fused to mKate2; Bottom, mCitrine fused to mCherry. Signal-weighted α images from single pixel fitting are also shown. Total TCSPC counts were $N \simeq 5 \times 10^6$. Images are 512×512. Scale bars are 20 μm. A slightly lower α value ($\alpha = 0.388 \pm 0.011$, $\tau_1 = 2.596 \pm 0.011$, $\tau_2 = 1.086 \pm 0.024$ for $N \simeq 5 \times 10^6$ counts) was obtained for donor mTFP1 fused to acceptor mCitrine (not shown).

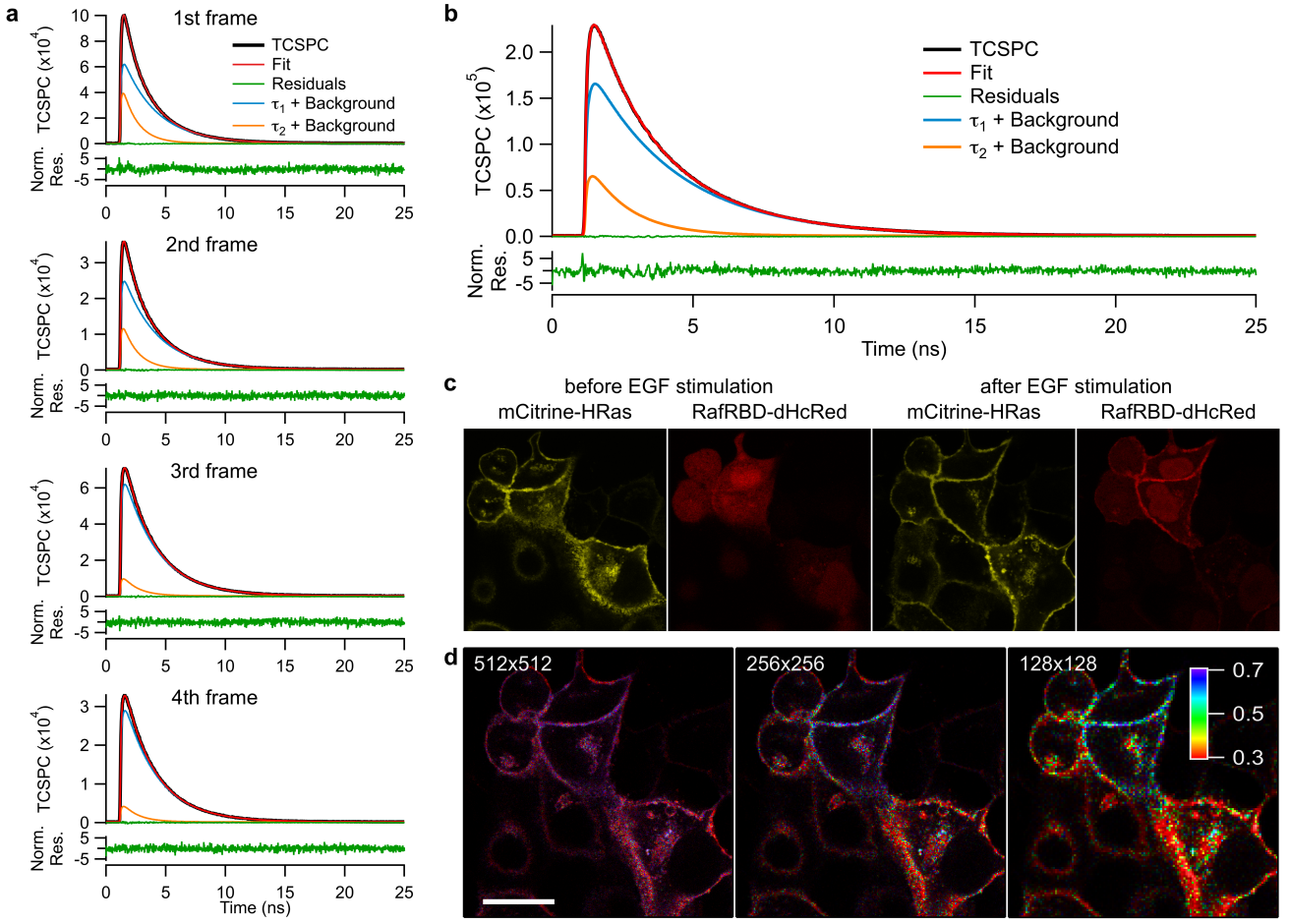

Fig. S13 TCSPC χ^2 fits and controls for Caspase3 sensor and HRas/RafRBD experiments. **(a)** Histogram fits for the four timepoints shown in Fig. 3a. Integration times for each frame from top to bottom (from left to right in Fig. 3a) were 11.0 min ($N \simeq 1.7 \times 10^7$ counts), 7.5 min ($N \simeq 6.4 \times 10^6$ counts), 10.9 min ($N \simeq 1.4 \times 10^7$ counts), and 4.7 min ($N \simeq 6.7 \times 10^6$ counts). Lifetimes of $\tau_1 = 2.810 \pm 0.002$ ns and $\tau_2 = 1.257 \pm 0.006$ ns were determined by global analysis of all frames. Only the IRF model parameters and α were allowed to vary for each frame, resulting in $\alpha = 0.412 \pm 0.001$, 0.338 ± 0.001, 0.145 ± 0.001, and 0.135 ± 0.002 (from top to bottom). The τ_1 value agreed (within a few percent) with the monoexponential value obtained for freely-diffusing mCitrine *in vivo* (see Table 1). τ_1 and τ_2 also agreed well with the lifetimes obtained for the uncleavable construct (Fig. S12). **(b)** TCSPC χ^2 fit of the entire 7 min integration (2 min before EGF addition plus 5 min after EGF addition) from which the frames shown in Fig. 3b were taken. Lifetime values were $\tau_1 = 3.097 \pm 0.004$ ns, $\tau_2 = 1.442 \pm 0.011$ ns, and $\alpha = 0.300 \pm 0.004$ ($N \simeq 4.5 \times 10^7$ counts). The τ_1 value agreed well with cells expressing only mCitrine-HRas (mono-exponential $\tau = 2.974 \pm 0.002$ ns, $N \simeq 5 \times 10^6$ counts). **(c)** Images of cells before and after addition of EGF (final image taken immediately after the FLIM acquisition). Stimulation by EGF leads to recruitment of RafRBD-dHcRed to mCitrine-HRas. Cells in the upper left expressed a high ratio of acceptor to donor, which explains why only these cells experienced a significant lifetime decrease. **(d)** Rebinning of images allowed improved assessment of α at the same time resolution. The final frame from Fig. 3b is redisplayed at its original resolution of 512×512 (left, signal $S \simeq 47$ in brightest pixel), and at 256×256 (middle, signal $S \simeq 165$ in brightest pixel) and 128×128 (right, signal $S \simeq 518$ in brightest pixel).

Table S1 TCSPC χ^2 fit values for Monte Carlo biexponential data in Fig. S5.

λ (nm)	input α	τ_1 (ns)	τ_2 (ns)	α
405	0.2	3.008 ± 0.014	1.505 ± 0.068	0.205 ± 0.018
	0.5	3.009 ± 0.019	1.526 ± 0.023	0.506 ± 0.013
	0.8	2.981 ± 0.031	1.499 ± 0.010	0.796 ± 0.008
440	0.2	2.986 ± 0.012	1.413 ± 0.066	0.190 ± 0.015
	0.5	2.974 ± 0.016	1.454 ± 0.022	0.488 ± 0.012
	0.8	2.982 ± 0.031	1.490 ± 0.010	0.796 ± 0.008
470	0.2	3.009 ± 0.015	1.561 ± 0.070	0.209 ± 0.020
	0.5	2.979 ± 0.016	1.472 ± 0.021	0.487 ± 0.012
	0.8	3.002 ± 0.031	1.502 ± 0.010	0.801 ± 0.008
532	0.2	2.994 ± 0.013	1.451 ± 0.065	0.194 ± 0.016
	0.5	3.012 ± 0.018	1.527 ± 0.022	0.506 ± 0.013
	0.8	3.011 ± 0.032	1.509 ± 0.010	0.803 ± 0.008